# Impact of Heterometallic Cooperativity of Iron and Copper Active Sites on Electrocatalytic Oxygen Reduction Kinetics

*Masaru Kato,*[*,†,‡,§] *Natsuki Fujibayashi,*[‡] *Daiki Abe,*[‡] *Naohiro Matsubara,*[‡] *Satoshi Yasuda,*[||] *Ichizo Yagi**[*,†,‡,§]

[†]Faculty of Environmental Earth Science and [‡]Graduate School of Environmental Science, Hokkaido University, N10W5, Kita-ku, Sapporo 060-0810, Japan

[||] Research Group for Nanoscale Structure and Function of Advanced Materials, Advanced Science Research Center, Japan Atomic Energy Agency, 2-4 Shirakata, Tokai, Ibaraki 319-1195, Japan

[§] Global Research Center for Environment and Energy based on Nanomaterials Science (GREEN), National Institute for Materials Science (NIMS), Tsukuba 305-0044, Japan

**ABSTRACT.** The oxygen reduction reaction (ORR) is a key reaction in polymer electrolyte fuel cells and metal–air batteries. In these electrochemical systems, platinum group metals (PGMs) have been widely used as ORR electrocatalysts. Because of material costs and scarcity of platinum group metals, non-PGM electrocatalysts are an ideal alternative for mass production with low material costs. Many non-PGM electrocatalysts have been intensively studied such as pyrolyzed Fe-, N-doped carbon (Fe–N–C) catalysts. However, many non-PGM electrocatalysts including Fe–N–C still suffer from product selectivity: the production of $H_2O_2$ as the byproduct. In this work, we synthesized an ORR electrocatalyst of Cu-, Fe- and N-doped carbon nanotubes, (Cu,Fe)–N–CNT. This heterobimetallic catalyst showed the selective $4e^-$ reduction of $O_2$ to $H_2O$ with ca. 99%. Kinetic analysis of the electrocatalytic ORR and hydrogen peroxide reduction reaction (HPRR) in acidic media revealed that (Cu,Fe)–N–CNT showed two orders of magnitude higher rate constants for the direct $4e^-$ reduction of $O_2$ to $H_2O$ than those for the $2e^-$ reduction of $O_2$ to $H_2O_2$ whereas a monometallic Fe–N–CNT showed the same order of magnitude, indicating that the heterometallic cooperativity gave the drastic impact on the ORR kinetics. Our findings would open up possibilities to develop non-PGM ORR electrocatalysts with heterobimetallic active sites for the selective ORR.

KEYWORDS. Non-PGM, oxygen reduction reaction, electrocatalysis, polymer electrolyte fuel cell, oxygen reduction kinetics, bio-inspired approach, heterobimetallic active sites.

## Introduction

The oxygen reduction reaction (ORR) is a key reaction in polymer electrolyte fuel cells (PEFCs) and efficiently catalyzed by platinum group metal (PGM)-based electrocatalysts. Since ca. 56% of the cost in a fuel cell stack comes from expensive PGMs,[1] developing highly active and durable ORR electrocatalysts based on earth-abundant elements is necessary for large-scale production of PEFCs. Metal–nitrogen–carbon (M–N–C) electrocatalysts containing earth abundant metals are promising alternatives to PGM-based ORR electrocatalysts[2] and especially Fe–N–C electrocatalysts have been intensively studied because they show relatively high electrocatalytic activity even in acidic media.[3-16]

The production of $H_2O_2$ as the byproduct for the ORR is a major concern in many non-PGM electrocatalysts including Fe–N–C. The $4e^-$ reduction of $O_2$ produces $H_2O$ whereas partial $2e^-$ reduction of $O_2$ gives $H_2O_2$. Low product selectivity of ORR electrocatalysts is believed to contribute to the degradation of the catalyst and/or ionomer and proton-exchange membranes in PEFCs through Fenton-type side reactions, which generate radical species particularly from Fe ion species and $H_2O_2$ ($Fe^{2+}/H_2O_2 \rightarrow Fe^{3+}/\bullet OH/OH^-$, $Fe^{3+}/H_2O_2 \rightarrow Fe^{2+}/\bullet OOH/H^+$).[3-5,17] The improvement of the $4e^-$ selectivity is crucial for developing practical non-PGM catalysts. To improve the ORR activity and selectivity of Fe–N–C, heterometal-doped Fe–N–C catalysts of (M,Fe)–N–C (M = Mn,[18] Co,[19-20] Ni[21] or Cu[22-30]) have been synthesized.[31-32]

In nature, a highly selective non-PGM ORR catalysts with heterobimetallic active sites is known: a metalloenzyme of cytochrome *c* oxidase (C*c*O). The C*c*O is a transmembrane metalloenzyme and found in the inner mitochondrial membrane of eukaryotes and in the cytoplasmic membrane of prokaryotes. The C*c*O utilizes a binuclear complex containing a heme and a copper ion as the active center.[33-34] The selectivity to the $4e^-$ reduction for the ORR reaches

>99% for C*c*O.[35-36] Inspired by the active site structure of C*c*O, molecular-based C*c*O mimics have been synthesized to understand mechanistic insights into the enzymatic ORR. Electrochemical studies of these synthetic models suggest that the Cu site acts as the initial $O_2$ binding site to form bridging heme–peroxo–Cu intermediates and suppresses the release of reactive oxygen species.[16,37-40] Cu-doped Fe–N–C, (Cu,Fe)–N–C, electrocatalysts have also been synthesized for the ORR and synergistic effects of the copresence of iron and copper active sites on the ORR activity have been found.[22-30] Furthermore, the suppression of the $H_2O_2$ production was also observed for (Cu,Fe)–N–C electrocatalysts, compared with the corresponding Cu–N–C and Fe–N–C catalysts.[28] However, heterobimetallic effects of Cu and Fe active sites on the ORR kinetics remain unclear although intensive kinetic studies have been done for single metallic M–N–C catalysts such as Fe–N–C.[41-43]

Herein, we report synthesis, characterization and kinetic analysis of Cu-, Fe- and N-doped carbon nanotubes, (Cu,Fe)–N–CNT, for the ORR in acidic media. The bimetallic (Cu,Fe)–N–CNT electrocatalyst was synthesized in pyrolysis from a composite of chloro(protoporphyrinato)iron (hemin),[22,44] a trinuclear copper complex of Cutrz ($[Cu^{II}_3(trz)_3(\mu\text{-}OH)]Cl_2\cdot 6H_2O$, trz = 1,2,4-triazole)[45-46] and single-walled carbon nanotubes (SWCNTs), which originate from vertically aligned carbon nanotubes (VACNTs)[7,10] (**Scheme 1**). Inspired by the C*c*O binuclear active site of a heme and a copper complex of histidine ligands, hemin and Cutrz were used as metal precursors. SWCNTs can be expected to enable the immobilization of a large amount of catalytic active sites on individual SWCNT surfaces.[7,10,20,47] Electrochemical measurements and kinetic analysis of (Cu,Fe)–N–CNT for not only the ORR but also the hydrogen peroxide reduction reaction (HPRR) allowed us to determine electrochemical inherent rate constants and turnover frequencies (TOFs) of the direct $4e^-$ reduction process of $O_2$ to $H_2O$.

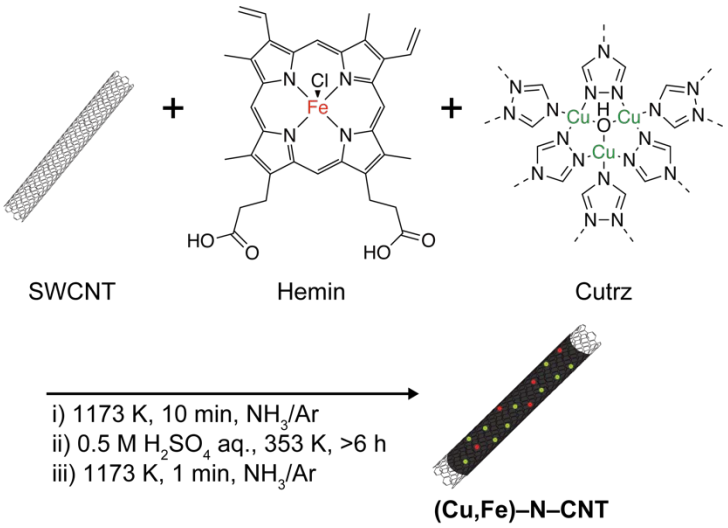


**Scheme 1**. Synthesis of our (Cu,Fe)–N–CNT ORR electrocatalyst.

## Experimental Section

**Material.** SWCNTs (ZEONANO SG101) were provided by ZEON Co., Ltd. A 5% Nafion® 117 dispersion and hemin (chloro(protoporphyrinato)iron(III) from bovine, ≧90%) were purchased from Wako Pure Chemical Industries Ltd. and Sigma-Aldrich, respectively. $[Cu^{II}_3(trz)_3(\mu\text{-}OH)]Cl_2 \cdot 6H_2O$ (Cutrz) was prepared according to the literature.[45] Ultrapure oxygen (purity, 99.9999%) and ultrapure argon (purity, >99.9995%) were used for all electrochemical measurements.

**Preparation of copper–iron–nitrogen-doped carbon nanotubes, (Cu,Fe)–N–CNT.** SWCNTs (4.0 mg) were dispersed in $CH_2Cl_2$ (30 mL) using a homogenizer (Branson Analog Sonifier® 250A, Branson Ultrasonics Corporation) for 30 min (output control: 40 W; duty cycle: 50%) in

an ice–water mixture. A dispersion of hemin (15.7 mg 24.1 μmol) in $CH_2Cl_2$ (2.4 mL) was sonicated for ca. 5 min and then this dispersion was slowly added to the dispersion of SWCNTs, followed by ultrasonication for ca. 30 min in an ice–water mixture. To the dispersion of hemin/SWCNT, a dispersion of Cutrz (9.4 mg, 15.9 μmol) in EtOH (5 mL) was added to obtain a nanocomposite with a 2:1 Cu–Fe atomic ratio. The mixture was sonicated for ca. 30 min in an ice–water mixture. The solvent was evaporated at 373 K in a vacuum for a couple of hours, yielding ca. 20 mg of Cutrz/hemin/SWCNT composite.

For heat treatments, the composite of Cutrz/hemin/SWCNT (10 mg) was placed in a carbon crucible (26 mm in OD, 20 mm in ID and 20 mm in height) and then heated in the reaction chamber of an electromagnetic inductive heating furnace (MU-1700D, SK Medical Electronics Co., Ltd.) in 0.45% $NH_3$/Ar. In the first heating process, heating temperatures was held at 473 K for 10 min, raised to 1173 K at a ramp rate of 523 K $min^{-1}$ and then kept at 1173 K for 10 min. After the heat treatment, the reaction chamber was naturally cooled down to room temperature, giving ca. 6.5 mg of the as-heated catalyst.

The as-heated catalyst was stirred in 0.5 M $H_2SO_4$ aqueous solution at 353 K overnight. The precipitate was collected by vacuum filtration, washed with Milli-Q water and then dried at 373 K in a vacuum for at least 2 h. In the second heating process, the acid-treated product (10 mg) was heated at 473 K for 10 min, raised to 1173 K at a ramp rate of 523 K $min^{-1}$ and then kept at 1173 K for 1 min to obtain the final product of (Cu,Fe)–N–CNT (ca. 10 mg). Elemental analysis: C, 87.46 wt%; H, <0.30 wt%; N, 2.86 wt%. ICP–AES analysis: Cu, 0.58 wt%; Fe, 1.20 wt%.

To optimize synthetic conditions, we prepared (Cu,Fe)–N–CNT with changing amounts of Cutrz: 4.7 mg of Cutrz (7.96 μmol) (Cu:Fe= 1:1 in the atomic ratio in the precursor mixture);

18.8 mg of Cutrz (31.82 μmol) (Cu:Fe= 4:1). We also prepared catalysts at different temperatures of 1073 and 1273 K. To optimize heating periods, catalysts were prepared at 1173 K for 5, 7, 10, 12 min in the first heating step.

**Preparation of iron-nitrogen-doped carbon nanotubes, Fe–N–CNT.** A composite of SWCNTs (4.0 mg) and hemin (15.7 mg 24.1 μmol) was used as the precursor and treated in the same manner as (Cu,Fe)–N–CNT. Yield: ca. 12 mg. Elemental analysis: C, 91.79 wt%; H, <0.30 wt%; N, 1.64 wt%. ICP-AES analysis: Fe, 0.96 wt%.

**Preparation of copper-nitrogen-doped carbon nanotubes, Cu–N–CNT.** A composite of SWCNTs (4.0 mg) and Cutrz (9.4 mg, 15.9 μmol) was dispersed in $CH_2Cl_2$ (ca. 30 mL) using a homogenizer (Branson Analog Sonifier® 250A, Branson Ultrasonics Corporation) for 70 min (output control: 40 W; duty cycle: 50%) in an ice–water mixture. After that, the dispersion was treated in the same manner as (Cu,Fe)–N–CNT. Yield: ca. 3.5 mg. Elemental analysis: C, 95.83 wt%; H, <0.30 wt%; N, 0.68 wt%. ICP-AES analysis: Cu: 0.08 wt%.

**Preparation of heat- and acid-treated carbon nanotubes, non-doped CNT.** SWCNTs (10.0 mg) were treated in the same manner as (Cu,Fe)–N–CNT. Yield: ca. 7.5 mg.

**Characterization**. X-ray photoelectron spectra of catalysts were collected on a photoelectron spectrometer of JPS-9200 (JEOL) using an Al $K_\alpha$ X-ray source. The peak of C=C in the C1s region was used as the internal standard (284.8 eV) to calibrate the binding energies of the elements. Powder X-ray diffraction data were collected on an X-ray diffractometer (MiniFlex, Rigaku) with graphite monochromatized Cu $K_\alpha$ radiation ($\lambda$ = 0.1540562 nm) at 30 kV and 15 mA. A scanning rate was set to $2^o$/min. Data on inductively coupled plasma atomic emission spectroscopy (ICP-AES) were collected on an ICP-AES spectrometer ICPE-9000 (Shimadzu Corporation). For the

sample preparation for ICP-AES, the catalyst was added in a 1 M $HNO_3$ aqueous solution, and then left at room temperature overnight. The residue was removed with a membrane filter (0.45 μm) and then the filtrate was diluted with Milli-Q water to prepare sample solutions in 0.1 M $HNO_3$ aqueous solution. Elemental analysis was done at Global Facility Center, Hokkaido University. High-angle annular dark field (HAADF)−scanning transmission electron microscopy (STEM) images and energy dispersive X-ray spectroscopy (EDS) mapping for iron nanoparticles were taken using a JEOL JEM-ARM200F instrument at 80 kV. $N_2$ adsorption and desorption isotherms of (Cu,Fe)–N–CNT were recorded at 77 K using BELSORP mini II (MicrotracBEL Corp.) to determine a specific surface area of it based on Brunauer–Emmett–Teller (BET) analysis. The sample was pretreated at 423 K under vacuum for 24 h before measurements. To measure water contact angles, the $\theta/2$ method was used.[48] Milli-Q water (10 μL) was drop-cast on a substrate, and then photographs from the side at the interface between the water droplet and the substrate were taken. Water contact angles of $\theta$ were determined from angles of $\theta/2$ between two lines: one is parallel to the substrate surface and the other is the line between the apex of the water droplet and the contact point at the edge of the water droplet and the substrate. For (Cu,Fe)–N–CNT, a catalyst ink, which was prepared in the same way for electrochemical measurements mentioned below, was drop-cast onto a glassy carbon substrate and dried.

**Electrochemistry.** All electrochemical data were collected using a potentiostat of CompactStat (Ivium Technologies) with conventional three-electrode setups. An Ag|AgCl electrode in a saturated KCl aqueous solution was used as the reference electrode. All potentials were converted to the reversible reference electrode (RHE) using the following equation: $E_{RHE} = E_{Ag|AgCl} + 0.199 + pH \times 0.059$. All potentials shown *vs*. RHE were corrected with solution resistances of 45.2 Ω in a 0.05 M $H_2SO_4$ aqueous solution for the ORR and 49.0 Ω in a 0.05 M $H_2SO_4$ aqueous solution

containing $H_2O_2$ for the HPRR. These solution resistances were obtained in electrochemical impedance spectroscopy at +0.5 V *vs*. RHE using an ac amplitude of 10 mV in the frequency range from 1 kHz to 1 Hz with 8 points/decade (Biologic SP-240). A carbon rod was used as the counter electrode. As the working electrode, a catalyst-modified glassy carbon (GC) disk (5 mm in diameter) was used in a rotating ring-disk electrode (RRDE) tip, in which a Pt ring is also built.

For the electrode preparation, a glassy carbon disk was sonicated in ethanol for 5 min, polished with 1.0 μm diamond suspension (Maruto Instrument), followed by 0.25 μm diamond suspension (Maruto Instrument), and then sonicated in Milli-Q water for 5 min. A catalyst ink containing 2.0 mg of a catalyst, 40 μL of ethanol, 160 μL of Milli-Q water and 1 μL of 5% Nafion® 117 dispersion was mixed with the homogenizer with the minimum power output and 50% duty cycle for 4 min in an ice–water mixture. The catalyst ink (13 μL) was drop-cast on a GC disk placed in the RRDE tip rotating at 500 rpm and dried for 50 min at room temperature at 500 rpm for standard electrochemical measurements (the loading density of the catalyst: 0.66 $mg_{cat.}$ $cm^{-2}$). To understand effects of catalyst loading densities on the ORR activity of each catalyst, the catalyst ink with 11 or 15 μL was also drop-cast onto the GC, giving catalyst densities of 0.56 or 0.76 $mg_{cat.}$ $cm^{-2}$, respectively. The ring electrode was electrochemically cleaned in 0.05 M $H_2SO_4$ aq. under Ar at a sweep rate of 100 mV $s^{-1}$ in the potential rage of +0.05 and +1.0 V *vs*. RHE for 50 cycles before use. Linear sweep voltammograms (LSVs) for the ORR were recorded at a sweep rate of 10 mV $s^{-1}$ in 0.05 M $H_2SO_4$ aq. at pH 1 under oxygen, applying a potential of +1.2 V *vs*. RHE to the ring electrode. A collection efficiency of the ring electrode was experimentally determined to be 0.20 and this value was used for data analysis. The collection efficiency was determined using a gold disk electrode (5 mm in diameter) in the RRDE in 0.05 M $H_2SO_4$ aq. containing 2 mM $K_3[Fe(CN)_6]$ under Ar, applying +0.97 V *vs*. RHE to the ring electrode. Yields

of $H_2O_2$ produced in LSVs were calculated as follows: $H_2O_2$ yield (%) = (200 x $I_R/N$) / ($|I_D|$ + $I_R/N$), where $I_R$, $I_D$ and $N$ are the ring current, disk current and collection efficiency (0.20), respectively. For durability tests, 5,000 potential cycles in the potential range between +0.6 and +1.0 V vs. RHE were repeated at a sweep rate of 100 mV $s^{-1}$ in 0.05 M $H_2SO_4$ aq. under oxygen. For the HPRR, the catalyst ink was drop-cast and dried on a GC screw (5 mm in diameter, M4, Tokai Carbon Co. Ltd.) in the same manner as the use of the GC disk and then heated at 418 K for 5 min to improve the adhesion between the catalyst film and the GC surface.[46] LSVs were recorded in 0.05 M $H_2SO_4$ aq. containing $H_2O_2$ under Ar. The concentration of $H_2O_2$ in the electrolyte solution was determined by the titration of 5 mM $KMnO_4$ aqueous solution before and after the electrochemical measurements to be 3.2 mM for (Cu,Fe)–N–CNT, 3.0 mM for Fe–N–CNT and 3.2 mM for Cu–N–CNT.

To calculate the maximum mass-based site density (MSD) for (Cu,Fe)–N–CNT, cyclic voltammograms of (Cu,Fe)–N–CNT were recorded in 0.05 M $H_2SO_4$ aq. under Ar to extract peak current densities of redox couples of redox-active metal species such as $Fe^{III}/Fe^{II}$ and $Cu^{II}/Cu^{I}$ based on extrapolated baselines.[7] The extracted peak current densities allowed us to calculate Faradaic charge densities involving redox reactions. The charge densities can be converted to the number of redox-active sites in the catalyst immobilized on the electrode by using the Faraday constant ($F$ = 96500 C $mol^{-1}$), the Avogadro constant ($N_A$ = 6.02 × $10^{23}$ $mol^{-1}$) and a catalyst density (0.66 $mg_{cat.}$ $cm^{-2}$). To determine a site density of active sites per surface area, the MSD was divided by a BET surface area of the catalyst.

**Determination of intrinsic currents and rate constants.**

To determine rate constants for the ORR and HPRR, LSVs for the ORR and HPRR using a RRDE at 1600 rpm were analyzed using the Nabae model.[41,49] A worksheet file in Microsoft Excel is

available on the website of the original paper on the Nabae model as the supporting information[41] and used for the data analysis of our data to extract kinetic parameters.

We performed ORR and HPRR measurements of a catalyst with different catalyst loading amounts. Koutechy-Levich (K–L) plots for the HPRR allowed us to determine a rate constant for the HPRR ($k_3$') from the intercept and $Z_2$ from the slope. $Z_2$ equal to $0.62D_{H_2O_2}^{2/3}\nu^{-1/6}$ is a $H_2O_2$ diffusion parameter dependent on the diffusion coefficient of $H_2O_2$ and the viscosity of the electrolyte. From $k_3$', $Z_2$ and collected data on disk ($I_d$) and ring ($I_r$) currents of the RRDE for the ORR, we calculated currents for the direct 4e$^-$ reduction of $O_2$ to $H_2O$ ($I_1$'), the 2e$^-$ reduction of $O_2$ to $H_2O_2$ ($I_2$') and the 2e$^-$ reduction of $H_2O_2$ to $H_2O$ ($I_3$') using the following Eqs (1)–(3):

$$I_2' = \frac{1}{2}\left(\frac{I_r}{N} + \sqrt{\left(\frac{I_r}{N}\right)^2\left(1 + \frac{4k_3'}{Z_2\omega^{\frac{1}{2}}}\right)}\right) \quad (1)$$

$$I_3' = \frac{1}{2}\left(-\frac{I_r}{N} + \sqrt{\left(\frac{I_r}{N}\right)^2\left(1 + \frac{4k_3'}{Z_2\omega^{\frac{1}{2}}}\right)}\right) \quad (2)$$

$$I_1' = I_d - \sqrt{\left(\frac{I_r}{N}\right)^2\left(1 + \frac{4k_3'}{Z_2\omega^{\frac{1}{2}}}\right)} \quad (3)$$

where $N$ is the collection efficiency of the ring electrode (0.20 in this work), and $\omega^{-\frac{1}{2}}$ is the inverse square root of the angular frequency of the RDE rotated at 1600 rpm (0.1093 rad$^{-1/2}$ s$^{1/2}$ in this work). To convert $I_1$' and $I_2$' to rate constants of $k_1$' and $k_2$', the following Eqs 4 and 5 based on the K–L equation for the ORR to $H_2O$ and $H_2O_2$ were considered:

$$\frac{1}{I_1'} = \frac{1}{4AFc_{O_2}k_1'} + \frac{k_1'+k_2'}{4AFZ_1c_{O_2}k_1'}\omega^{-\frac{1}{2}} \quad (4)$$

$$\frac{1}{I_2'} = \frac{1}{2AFc_{O_2}k_2'} + \frac{k_1'+k_2'}{2AFZ_1c_{O_2}k_2'}\omega^{-\frac{1}{2}} \quad (5)$$

where $c_{O_2}$ is the concentration of $O_2$ in the bulk electrolyte solution ($1.05\times10^{-6}$ mol cm$^{-3}$), and $Z_1 = 0.62D_{O_2}^{2/3}\nu^{-1/6}$ (0.000776 cm s$^{-1/2}$) is a parameter calculated from the diffusion coefficients of $O_2$ and the kinetic viscosity of the electrolyte. These Eqs. 4 and 5 can be simultaneously solved because $I_1$', $I_2$' and the other parameters are known:

$$\frac{1}{k_1'} = \frac{4AFc_{O_2}}{I_1'} - \frac{1+\frac{2I_2'}{I_1'}}{Z_1\omega^{\frac{1}{2}}} \qquad (6)$$

$$k_2' = \frac{2I_2'}{I_1'}k_1' \qquad (7)$$

To exclude the contribution of a quasi-four-electron pathway (also known as a dual site 2×2e$^-$ pathway), $I_1$'/($I_1$'+2$I_2$') values were plotted as a function of catalyst loading densities, $\gamma$ in μg cm$^{-2}$. It was assumed that intrinsic currents of $I_1{}^0$, $I_2{}^0$ and $I_3{}^0$ are first-order in γ because these parameters show the intrinsic proportions of the individual chemical reactions whereas $I_s$, which is the current that originates from the series of reactions in the catalyst layer matrix, is second-order in $\gamma$ because the reactant must react twice over the catalyst to complete the ORR to $H_2O$ in the catalyst layer matrix. The correlation between $I_1$' and γ can be shown in the following Eq. 8:

$$\frac{I_1'}{I_1'+2I_2'} = \frac{I_1^0}{I_1^0+2I_2^0} + \frac{2I_s}{I_1^0+2I_2^0} = a + b\gamma \qquad (8)$$

The plot of $I_1$'/($I_1$'+2$I_2$') against γ gave the intercept of $a$, which is independent of $\gamma$ and then intrinsic currents of $I_1{}^0$, $I_2{}^0$ and $I_3{}^0$ were obtained using the following Eqs. 9–11:

$$I_1^0 = a(I_1' + 2I_2') \qquad (9)$$

$$I_2^0 = \frac{I_1'+2I_2'-I_1^0}{2} \qquad (10)$$

$$I_3^0 = I_d - I_1^0 - I_2^0 \qquad (11)$$

Finally, the intrinsic rate constants of $k_1{}^0$ and $k_2{}^0$ were obtained from the Eqs 12–13.

$$\frac{1}{k_1^0} = \frac{4AFc_{O_2}}{I_1^0} - \frac{1+\frac{2I_2^0}{I_1^0}}{Z_1\omega^{\frac{1}{2}}} \qquad (12)$$

$$k_2^0 = \frac{2I_2^0}{I_1^0} k_1^0 \qquad (13)$$

Note that $k_3{}^0$ is the same as $k_3$' in this loading density correction. Thus,

$$k_3^0 = k_3' \qquad (14)$$

**Results and Discussion**

Firstly, we optimized synthetic conditions of (Cu,Fe)–N–CNT. This catalyst was prepared from composites of Cutrz, hemin and SWCNT in pyrolysis (**Scheme 1**). Different mixing ratios of Cutrz to hemin gave different electrocatalytic activity for the ORR (**Figure 1**). Pyrolyzed (Cu,Fe)–N–CNT catalysts were prepared from precursors with different atomic ratios of Cu to Fe, 2:1, 1:1, 4:1 and 1:0.5. The LSV of the catalyst prepared from the precursor mixture with the 2:1 Cu–Fe ratio showed the most positive onset potential for the ORR in them, indicating that this Cu–Fe ratio maximized the ORR electrocatalytic activity. We also optimized heating temperatures and periods for the synthesis of (Cu,Fe)–N–CNT from the precursor mixture with the 2:1 Cu–Fe ratio: heating temperatures at 1073, 1173 and 1273 K; heating periods in the first heating step for 5, 7, 10 and 12 min. The heat treatment at 1173 K for 10 min gave the highest catalytic activity for the ORR (**Figures S1** and **S2**). The (Cu,Fe)–N–CNT electrocatalyst that was prepared in the optimized condition (the 2:1 Cu–Fe atomic ratio in the precursor and the heating temperature of 1173 K for 10 min) showed ca. 1% $H_2O_2$ production yield, suggesting that (Cu,Fe)–N–CNT selectively catalyzes the ORR to $H_2O$. (Cu,Fe)–N–CNT prepared in the optimized condition was used for the further studies.

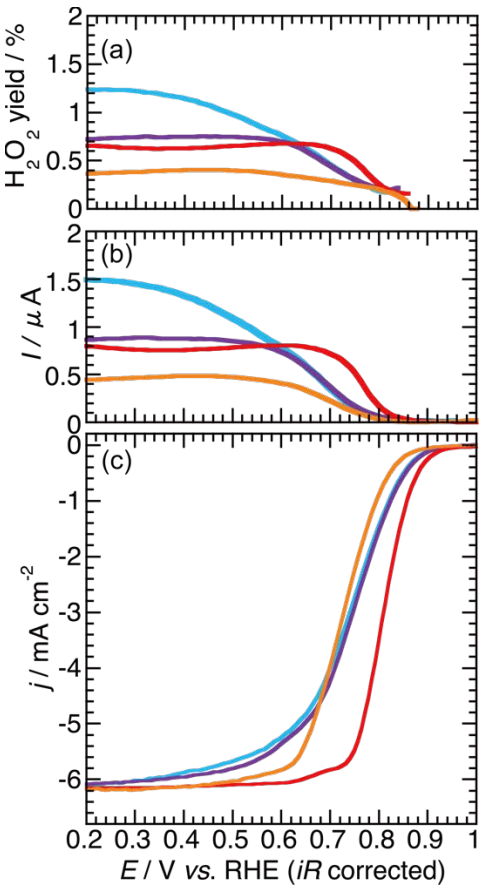


**Figure 1.** (a) $H_2O_2$ yield, (b) ring and (c) disk currents of (Cu,Fe)–N–CNT electrocatalysts that were prepared from precursors with different molar ratios of Cutrz to hemin: 2:1 Cu–Fe (in red), 1:1 (in purple), 4:1 (in orange) and 1:0.5 (in light blue) at 1173 K. The LSVs were recorded at 10 mV $s^{-1}$ using a RRDE at 1600 rpm in 0.05 M $H_2SO_4$ aqueous solution under oxygen. The catalyst loading density was 0.66 $mg_{cat}$ $cm^{-2}$.

Physicochemical measurements of (Cu,Fe)–N–CNT were performed for characterization. (Cu,Fe)–N–CNT had a BET surface area of 537 $m^2$ $g^{-1}$ (**Figure S3**) and a contact angle of ca. 156º (**Figure S4**). HAADF–STEM images of the catalyst showed a tubular morphology, which originates from that of SWCNTs (**Figures 2a** and **2b**). The combination of HAADF–STEM observation, EDS mapping and a powdery XRD pattern of (Cu,Fe)–N–CNT confirmed that Fe

nanoparticles surrounded by a continuous graphitic layer[8,11] remain even after the acid treatment (**Figure S5**). In contrast, no Cu nanoparticles were found in (Cu,Fe)–N–CNT because Cu nanoparticles can be easily removed with the acid treatment.[46] Elemental analysis and ICP-AES allowed us to determine atomic ratios of N:Cu:Fe = 22:1:2 (2.86:0.58:1.20 in wt%). The peak deconvolution analysis[6] of the X-ray photoelectron spectra of (Cu,Fe)–N–CNT in the N1s region showed 45% pyridinic and 28% pyrrolic nitrogen species in it (**Figure 2c** and **Table S1**). These nitrogen atoms have a lone pair of electrons and work as donation atoms to form $MN_x$ active sites.[6] The peak deconvolution analysis also suggests that ca. 18% of nitrogen atoms were used to form $MN_x$ active sites.

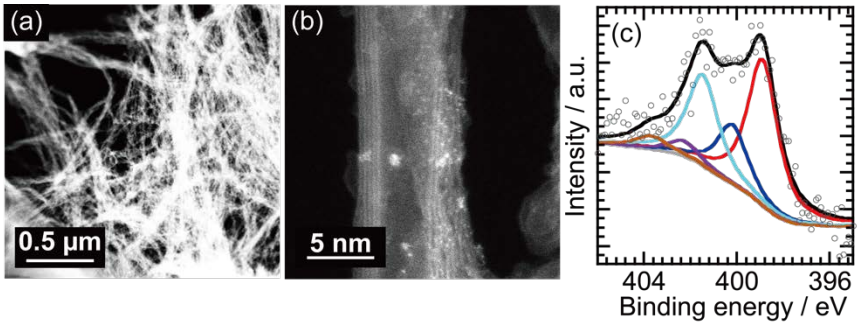


**Figure 2.** (a, b) HAADF–STEM images and (c) N1s X-ray photoelectron spectrum of (Cu,Fe)–N–CNT. Open circles: experimental data; the solid line in black: fitted data; the solid line in red: pyridinic nitrogen; the solid line in blue: nitrogen atoms coordinated to metal ions ($MN_x$); the solid line in light blue: pyrrolic nitrogen; the solid line in purple: graphitic nitrogen; the solid line in brown: N oxide; the solid line in gray: baseline.

The (Cu,Fe)–N–CNT electrocatalyst showed the synergistic effects of iron and copper active sites on the ORR activity. Fe–N–CNT, Cu–N–CNT and non-doped CNT were prepared from hemin/SWCNT, Cutrz/SWCNT and SWCNT, respectively. The comparison between LSVs of (Cu,Fe)–N–CNT, Cu–N–CNT and Fe–N–CNT under oxygen revealed that (Cu,Fe)–N–CNT

exhibited the most positive half potential, $E_{1/2}$ (**Figure 3**). Thus, (Cu,Fe)–N–CNT showed higher ORR activity than Cu–N–CNT and Fe–N–CNT. Similar synergistic effects on the ORR activity were also reported for (Cu,Fe)–N–C electrocatalysts.[22-30]

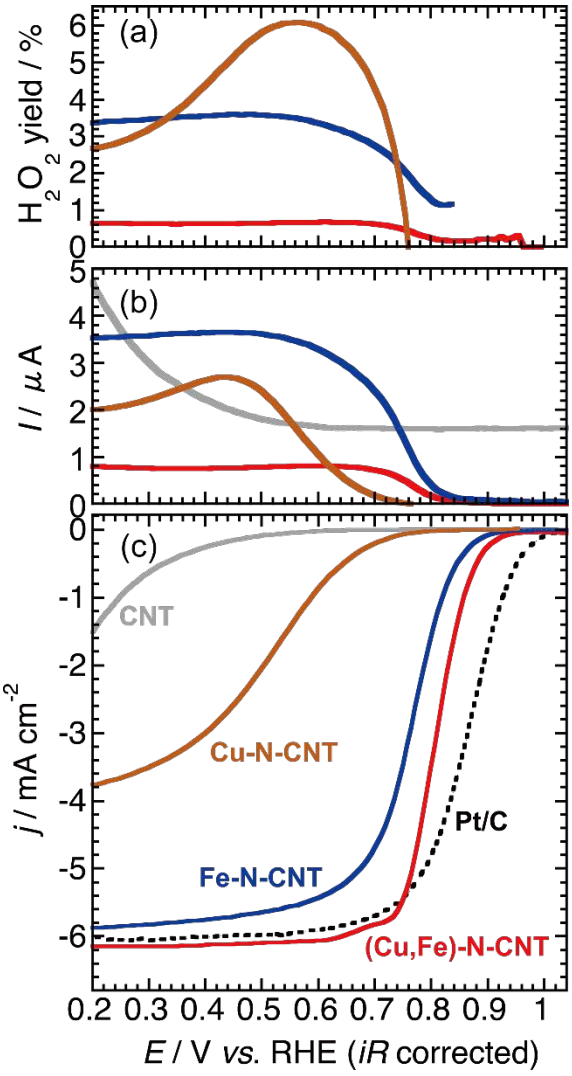


**Figure 3**. (a) $H_2O_2$ yield, (b) ring and (c) disk currents of (Cu,Fe)–N–CNT (the solid line in red), Cu–N–CNT (the solid line in brown), Fe–N–CNT (the solid line in blue), non-doped CNT (the solid line in gray) and Pt/C (the dotted line in black) recorded undergoing the negative sweep at 10 mV $s^{-1}$ in 0.05 M $H_2SO_4$ aqueous solution under oxygen except for Pt/C, which was recorded

undergoing positive sweep in 0.1 M $HClO_4$ aqueous solution under oxygen instead of $H_2SO_4$ aq. to avoid bisulfate adsorption.[50] A bias potential of +1.2 V *vs*. RHE was applied to the ring electrode. A catalyst loading density was 0.66 $mg_{cat.}$ $cm^{-2}$.

The (Cu,Fe)–N–CNT electrocatalyst tends to show higher product selectivity to $H_2O$ for the ORR than Fe–N–CNT and Cu–N–CNT. The copresence of iron and copper active sites could minimize the $H_2O_2$ production like C*c*O, which shows >99% selectivity for the four-electron ORR.[35-36] Note that the onset potential of Cu–N–CNT for the ORR is much more negative than that for Fe–N–CNT, suggesting that the ORR mainly occurs at iron sites and copper sites help them to accelerate the ORR. Such ORR mechanism was previously proposed for (Cu,Fe)–N–C electrocatalysts[23,29] and biomimetic molecular catalysts of the active site of C*c*O.[37-39] The LSV of non-doped CNT showed much lower ORR activity than the others, suggesting that the heat treatment of only SWCNTs produces no active sites. Note that durability tests of 5,000 potential cycles in the potential range between +0.6 and +1.0 V *vs*. RHE under oxygen for (Cu,Fe)–N–CNT, Cu–N–CNT and Fe–N–CNT revealed that (Cu,Fe)–N–CNT showed the lowest $E_{1/2}$ shift ($\Delta E_{1/2}$) value of ~20 mV (**Figure S6**), suggesting that the (Cu,Fe)–N–CNT showed the highest durability. This high durability could originate from the high product selectivity.

Interestingly, the comparison between LSVs of (Cu,Fe)–N–CNT and Pt/C undergoing the negative sweep revealed that these $E_{1/2}$ values for the ORR were the almost same (**Figure S7**). Generally, $E_{1/2}$ values of LSVs for PGM-based ORR electrocatalysts including Pt/C highly depend on the potential sweep direction and, their LSVs undergoing the negative sweep tends to show more negative $E_{1/2}$ than those undergoing the positive sweep since the surface of PGM catalysts can be covered with metal oxide or hydroxide species (M–O(H)) in oxidative conditions.[51-52] This

is the reason why representative LSVs of Pt/C are usually shown in the positive going sweep (**Figure 3**). However, in practice, ORR catalysts with higher catalytic activity undergoing the negative going sweep should be developed because PEFCs should provide the peak power for fuel cell vehicles during acceleration. Furthermore, the ORR activity is suppressed in the presence of sulfate ions, which can be produced by the degradation of perfluoro-sulfonic acid ionomers and inhibit the catalytic sites of platinum.[53-57] In contrast, (Cu,Fe)–N–CNT is tolerant to the sweep direction as well as sulfate ions. Thus, (Cu,Fe)–N–CNT would be a promising alternative to PGM-based electrocatalysts for the practical use in PEFCs.

To understand the cooperative effect of Fe and Cu active sites on ORR kinetics, rate constants at each step ($k_1^0$, $k_2^0$ and $k_3^0$) were determined for (Cu,Fe)–N–CNT, Cu–N–CNT and Fe–N–CNT in acidic media (**Figure 4** and **Table 1**), where $k_1^0$, $k_2^0$ and $k_3^0$ indicate rate constants of the direct 4e$^-$ reduction to $H_2O$ ($O_2 \rightarrow H_2O$), the 2e$^-$ reduction process of $O_2$ to $H_2O_2$ ($O_2 \rightarrow H_2O_2$) and the HPRR to $H_2O$ with 2e$^-$ transfer ($H_2O_2 \rightarrow H_2O$), respectively.[41] To determine $k_3$'(=$k_3^0$ in the Nabae model) values of each catalyst, LSVs for the HPRR were recorded in the presence of $H_2O_2$ in the electrolyte solution (**Figure S8**). Analysis of electrochemical results of the ORR and HPRR gave rate constants at each reaction process (**Figure 4a**) using the Nabae model.[41] This model enables us to exclude the contribution of a quasi-four-electron pathway (also known as a dual site 2×2e$^-$ pathway[1,8]) to the 4e$^-$ reduction process. Note that $I_1$'/($I_1$'+2$I_2$') values, where $I_1$' and $I_2$' are currents based on the Damjanovic model with a modified mathematical approach including the quasi-four-electron pathway,[41-42] seem to depend on the catalyst loading amount of Fe–N–CNT but not on that of (Cu,Fe)–N–CNT (**Figure S9**). It was also reported that the 2×2e$^-$ pathway was the main pathway for other Fe–N–

C electrocatalysts in acidic media.[49] Thus, the quasi-four-electron pathway is involved for Fe–N–CNT but not for (Cu,Fe)–N–CNT.

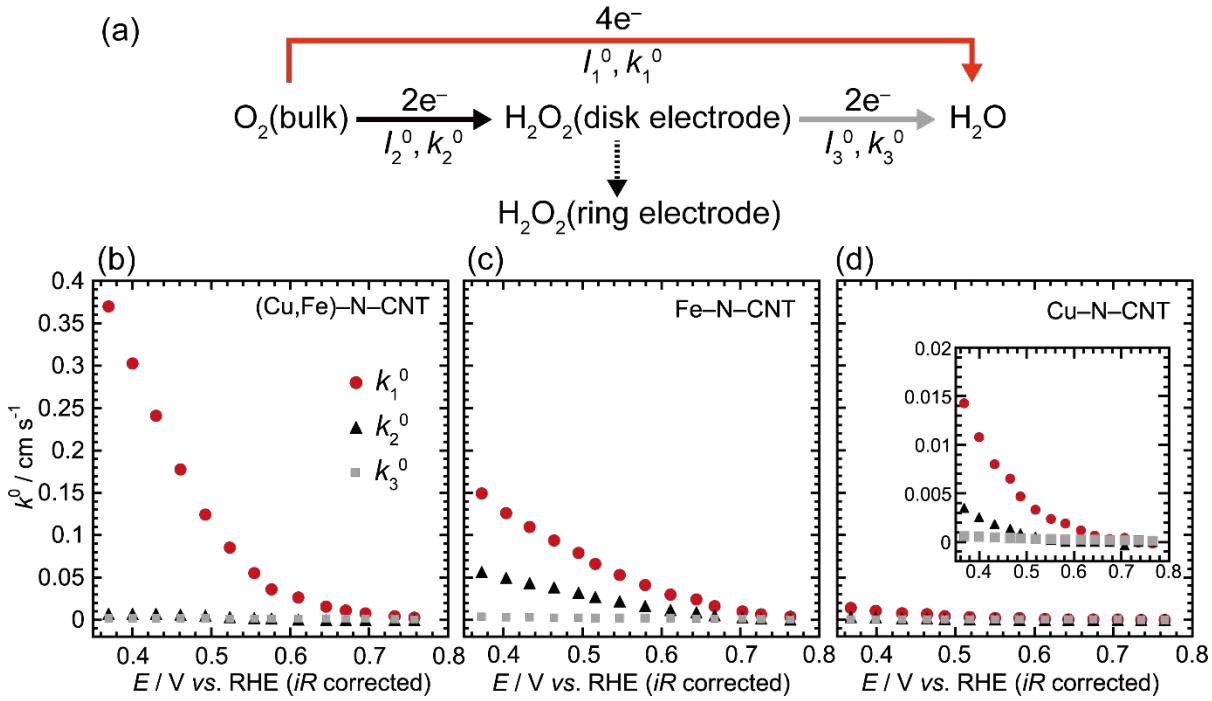


**Figure 4**. (a) ORR scheme with electrochemical inherent rate constants of $k_1^0$, $k_2^0$ and $k_3^0$ and $I_1^0$, $I_2^0$ and $I_3^0$ (Nabae model).[41,49] Rate constants of $k_1^0$ (the circles in red), $k_2^0$ (the triangles in black) and $k_3^0$ (the squares in gray) were plotted as a function of potential in 0.05 M $H_2SO_4$ aqueous solution for (b) (Cu,Fe)–N–CNT, (c) Fe–N–CNT and (d) Cu–N–CNT electrocatalysts (inset: a magnified graph of Cu–N–CNT). The contribution of the quasi-four-electron pathway (the dual site 2×2e⁻ pathway) to each rate constant was excluded using the Nabae model.[41]

**Table 1**. Electrochemical inherent rate constants of $k_1^0$, $k_2^0$ and $k_3^0$ of (Cu,Fe)–N–CNT, Fe–N–CNT and Cu–N–CNT for 0.66 $mg_{cat.}$ $cm^{-2}$ at +0.61 V *vs*. RHE in 0.05 M $H_2SO_4$ aqueous solution.

| Catalyst | $k_1^0$ / cm $s^{-}$ $_1$ | $k_2^0$ / cm $s^{-1}$ | $k_3^0$ / cm $s^{-1}$ |
|---|---|---|---|
| (Cu,Fe)–N–CNT | $2.6\times10^{-2}$ | $8.8\times10^{-4}$ | $1.8\times10^{-3}$ |
| Fe–N–CNT | $3.0\times10^{-2}$ | $1.2\times10^{-2}$ | $2.0\times10^{-3}$ |

| | | | |
|---|---|---|---|
| Cu–N–CNT | $1.2\times10^{-3}$ | $2.1\times10^{-5}$ | $2.9\times10^{-4}$ |

The kinetic analysis revealed that the copresence effect originates from the faster $4e^-$ transfer process. (Cu,Fe)–N–CNT showed much larger values of $k_1^0$ than that of $k_2^0$ ($k_1^0 >> k_2^0$), indicating that the direct $4e^-$ reduction pathway is exclusive (**Figure 4b** and **Table 1**). In the case of Fe–N–CNT, no such huge difference was observed between $k_1^0$ and $k_2^0$ (**Figure 4c** and **Table 1**), indicating that the $4e^-$and $2e^-$ reduction processes compete. In the case of Cu–N–CNT, rate constants of Cu–N–CNT are much smaller than those of (Cu,Fe)–N–CNT even though the direct $4e^-$ reduction process is dominant (**Figure 4d** and **Table 1**). These results suggest that Fe active sites exhibit larger rate constants for the ORR than copper active sites in acidic media and the copresence of Cu sites with Fe sites drastically accelerates the direct $4e^-$ reduction process.

Although further studies are needed to understand structural details on active sites of (Cu,Fe)–N–CNT, binuclear active sites of $FeN_4$ and $CuN_x$ might exist in the catalyst and exclusively catalyze the ORR to $H_2O$. One of the proposed active site structures is a binuclear metal active site placed in the same N-doped graphene sheets (**Figure S10a**),[20,32,58] where the ORR activity can be governed by simple geometric parameters such as metal–metal distances.[59] Heterobimetallic complexes with similar coordination environments have been reported.[60] We also propose another structure of heterobimetallic active sites: graphene sheets containing $FeN_4$ or $CuN_x$ active sites are stacked together (**Figure S10b**). The structure of $CuN_x$ active sites is based on the active site structure previously proposed for a Cu–N–C catalyst (r[Cutrz/GO]), which was prepared from Cutrz and graphene oxide and characterized by using HAADF–STEM and *in situ* X-ray absorption spectroscopy.[46] Since (Cu,Fe)–N–CNT was prepared from nanocomposites of Cutrz/hemin/SWCNT, the heat treatment could produce such a stacked

structure and $O_2$ molecules could be sandwiched between the two heterometallic active sites. Since the $k_1{}^0$ value for Fe–N–CNT is higher than that of Cu–N–CNT (**Table 1**), $FeN_4$ active sites serve as the main active site and are supported by $CuN_x$ active sites,[46] which could work as the initial $O_2$ binding site. Such a reaction mechanism is proposed for biomimetic C*c*O models to explain the suppression of the release of partially reduced oxygen species.[34,37-39]

Based on the kinetic analysis data, we estimated TOFs of (Cu,Fe)–N–CNT for the direct $4e^-$ transfer pathway. TOFs (*e* $site^{-1}$ $s^{-1}$) can be calculated from the following equation: TOF = ($J_{kin}$ × $N_A$) / ($F$ × MSD),[6-7,18,61] where $J_{kin}$ (A $g^{-1}$) is the kinetic current density, $N_A$ is the Avogadro constant ($6.02 \times 10^{23}$ $mol^{-1}$), $F$ is the Faradaic constant (96500 C $mol^{-1}$) and MSD is the mass-based site density. In this work, the kinetic current density calculated from $I_1{}^0$ using the Nabae model[41] was used as $J_{kin}$ to determine TOFs of the direct $4e^-$ reduction of $O_2$ for (Cu,Fe)–N–CNT. The MSD in this work was defined as the number of redox active sites per unit mass of the catalyst.[7,62] The MSD of (Cu,Fe)–N–CNT was electrochemically determined based on Faradaic charge densities of redox peaks observed in cyclic voltammograms recorded under Ar (**Figure S11**) to be $2.7 \times 10^{19}$ site $g_{cat.}{}^{-1}$. This MSD value and the BET surface area (537 $m^2$ $g_{cat.}{}^{-1}$) also allowed us to calculate the density of active sites per surface area to be $5.0 \times 10^{16}$ site $m^{-2}$ for (Cu,Fe)–N–CNT. The MSD and the total metal amount in the catalyst, which were determined by ICP–AES, gave a catalyst utilization factor[14,18] of ca. 15%. The MSD value and a $I_1{}^0$ value of 1.71 A $g^{-1}$ determined using the Nabae model for 0.66 $mg_{cat.}$ $cm^{-2}$ enabled us to calculate a TOF of 0.40 e $site^{-1}$ $s^{-1}$ at +0.80 V *vs*. RHE for the (Cu,Fe)–N–CNT catalyst. This TOF is comparable with previously reported TOFs of ca. 0.4 e $site^{-1}$ $s^{-1}$ at +0.8 V *vs*. RHE for Fe–N–C catalysts,[6-7] but less than those of ca. 1.5 e $site^{-1}$ $s^{-1}$ for (Fe,Mn)–N–C catalysts[18] and 11.4 e $site^{-1}$ $s^{-1}$ for a Fe–N–C catalyst.[63]

## Conclusions

The bimetallic (Cu,Fe)–N–CNT electrocatalyst showed high ORR catalytic activity and selectivity to the $4e^-$ reduction of $O_2$ to $H_2O$ (~99%). Kinetic analysis of the ORR and HPRR unveiled that the copresence of Fe and Cu active sites makes the direct $4e^-$ transfer pathway exclusive. The kinetic analysis also allowed us to determine the TOF of 0.40 e $site^{-1}$ $s^{-1}$ at +0.80 V *vs*. RHE for the direct $4e^-$ reduction pathway for (Cu,Fe)–N–CNT. This TOF is approximately 60 times smaller than a TOF of 25 e $site^{-1}$ $s^{-1}$ for Pt/C,[64] encouraging us to develop more active non-PGM electrocatalysts for the ORR. To develop (Cu,Fe)–N–CNT electrocatalysts with higher TOFs, synthetic approaches to non-PGM electrocatalysts with exclusive $MN_x$ moieties[6,47,65] coupled with our C*c*O-inspired approach would be promising. Although our work demonstrates the cooperative effect of different metal active sites on the ORR kinetics, the origin of the effect at the molecular level is still not fully understood. Spectroscopic studies such as *in situ* X-ray absorption spectroscopy are underway to gain mechanistic insights into the heterometallic cooperative effect.

## ASSOCIATED CONTENT

**Supporting Information**. The following files are available free of charge.

LSVs of electrocatalysts for the ORR and HPRR, $N_2$ adsorption and desorption isotherms, water contact angle measurements, STEM images, XRD pattern and proposed active site structures of (Cu,Fe)–N–CNT, plots of $I_1'/(I_1'+2I_2')$ as a function of catalyst loading density and a cyclic voltammogram of (Cu,Fe)–N–CNT recorded under Ar (PDF)

## AUTHOR INFORMATION

### Corresponding Author

*masaru.kato@ees.hokudai.ac.jp to MK. *iyagi@ees.hokudai.ac.jp to IY.

## ACKNOWLEDGMENTS

The authors thank Shingo Mukai and Yusuke Kawamura (Technical Division, Institute for Catalysis, Hokkaido University) for their technical support on electrochemical setups and Naomi Hirai and Yuko Mori (Research Institute for Electronic Science, Hokkaido University) for taking HAADF–STEM images. This work was supported by a Program for Development of Environmental Technology using Nanotechnology from the MEXT, Japan; Nanotechnology Platform Programs of MEXT at Hokkaido University; the Fusion-H program at Hokkaido University; Promotion for Young Research Talent and Network from Northern Advancement Center for Science & Technology (NOASTEC Japan); Grant-in-Aid for Young Scientists (B) (No. 16K20882 to MK); and Scientific Research (B) (No. 19H02664 to IY).

## ABBREVIATIONS

C*c*O, cytochrome *c* oxidase; (Cu,Fe)–N–CNT, Cu-, Fe- and N-doped carbon nanotube; HPRR, hydrogen peroxide reduction reaction; MSD, mass-based site density; ORR, oxygen reduction reaction; PEFC, polymer electrolyte fuel cell; PGM, platinum group metal; RRDE, rotating ring disk electrode; TOF, turnover frequency.

## REFERENCES

1. Wang, W.; Jia, Q. Y.; Mukerjee, S.; Chen, S. L. Recent Insights into the Oxygen-Reduction Electrocatalysis of Fe/N/C Materials. *ACS Catal.* **2019**, *9*, 10126-10141. DOI: 10.1021/acscatal.9b02583.
2. Bullock, R. M.; Chen, J. G.; Gagliardi, L.; Chirik, P. J.; Farha, O. K.; Hendon, C. H.; Jones, C. W.; Keith, J. A.; Klosin, J.; Minteer, S. D.; Morris, R. H.; Radosevich, A. T.; Rauchfuss, T. B.; Strotman, N. A.; Vojvodic, A.; Ward, T. R.; Yang, J. Y.; Surendranath, Y. Using nature's blueprint to expand catalysis with Earth-abundant metals. *Science* **2020**, *369*, eabc3183. DOI: 10.1126/science.abc3183.

3. Martinez, U.; Babu, S. K.; Holby, E. F.; Chung, H. T.; Yin, X.; Zelenay, P. Progress in the Development of Fe-Based PGM-Free Electrocatalysts for the Oxygen Reduction Reaction. *Adv. Mater.* **2019**, *31*, 1805157. DOI: 10.1002/adma.201806545.
4. Martinez, U.; Komini Babu, S.; Holby, E. F.; Zelenay, P. Durability challenges and perspective in the development of PGM-free electrocatalysts for the oxygen reduction reaction. *Curr. Opin. Electrochem.* **2018**, *9*, 224-232. DOI: 10.1016/j.coelec.2018.04.010.
5. Gewirth, A. A.; Varnell, J. A.; DiAscro, A. M. Nonprecious Metal Catalysts for Oxygen Reduction in Heterogeneous Aqueous Systems. *Chem. Rev.* **2018**, *118*, 2313-2339. DOI: 10.1021/acs.chemrev.7b00335.
6. Luo, F.; Choi, C. H.; Primbs, M. J. M.; Ju, W.; Li, S.; Leonard, N. D.; Thomas, A.; Jaouen, F.; Strasser, P. Accurate Evaluation of Active-Site Density (SD) and Turnover Frequency (TOF) of PGM-Free Metal–Nitrogen-Doped Carbon (MNC) Electrocatalysts using CO Cryo Adsorption. *ACS Catal.* **2019**, *9*, 4841-4852. DOI: 10.1021/acscatal.9b00588.
7. Yasuda, S.; Uchibori, Y.; Wakeshima, M.; Hinatsu, Y.; Ogawa, H.; Yano, M.; Asaoka, H. Enhancement of Fe–N–C carbon catalyst activity for the oxygen reduction reaction: effective increment of active sites by a short and repeated heating process. *RSC Adv.* **2018**, *8*, 37600-37605. DOI: 10.1039/C8RA08359B.
8. Choi, C. H.; Choi, W. S.; Kasian, O.; Mechler, A. K.; Sougrati, M. T.; Brüller, S.; Strickland, K.; Jia, Q.; Mukerjee, S.; Mayrhofer, K. J. J.; Jaouen, F. Unraveling the Nature of Sites Active toward Hydrogen Peroxide Reduction in Fe-N-C Catalysts. *Angew. Chem. Int. Ed.* **2017**, *56*, 8809-8812. DOI: 10.1002/anie.201704356.
9. Chung, H. T.; Cullen, D. A.; Higgins, D.; Sneed, B. T.; Holby, E. F.; More, K. L.; Zelenay, P. Direct atomic-level insight into the active sites of a high-performance PGM-free ORR catalyst. *Science* **2017**, *357*, 479-484. DOI: 10.1126/science.aan2255.
10. Yasuda, S.; Furuya, A.; Uchibori, Y.; Kim, J.; Murakoshi, K. Iron–Nitrogen-Doped Vertically Aligned Carbon Nanotube Electrocatalyst for the Oxygen Reduction Reaction. *Adv. Funct. Mater.* **2016**, *26*, 738-744. DOI: 10.1002/adfm.201503613.
11. Choi, C. H.; Baldizzone, C.; Polymeros, G.; Pizzutilo, E.; Kasian, O.; Schuppert, A. K.; Ranjbar Sahraie, N.; Sougrati, M.-T.; Mayrhofer, K. J. J.; Jaouen, F. Minimizing Operando Demetallation of Fe-N-C Electrocatalysts in Acidic Medium. *ACS Catal.* **2016**, *6*, 3136-3146. DOI: 10.1021/acscatal.6b00643.
12. Workman, M. J.; Serov, A.; Tsui, L.-k.; Atanassov, P.; Artyushkova, K. Fe–N–C Catalyst Graphitic Layer Structure and Fuel Cell Performance. *ACS Energy Lett.* **2017**, *2*, 1489-1493. DOI: 10.1021/acsenergylett.7b00391.
13. Li, J.; Ghoshal, S.; Liang, W.; Sougrati, M.-T.; Jaouen, F.; Halevi, B.; McKinney, S.; McCool, G.; Ma, C.; Yuan, X.; Ma, Z.-F.; Mukerjee, S.; Jia, Q. Structural and mechanistic basis for the high activity of Fe–N–C catalysts toward oxygen reduction. *Energy Environ. Sci.* **2016**, *9*, 2418-2432. DOI: 10.1039/C6EE01160H.
14. Leonard, N. D.; Wagner, S.; Luo, F.; Steinberg, J.; Ju, W.; Weidler, N.; Wang, H.; Kramm, U. I.; Strasser, P. Deconvolution of Utilization, Site Density, and Turnover Frequency of Fe–Nitrogen–Carbon Oxygen Reduction Reaction Catalysts Prepared with Secondary N-Precursors. *ACS Catal.* **2018**, *8*, 1640-1647. DOI: 10.1021/acscatal.7b02897.
15. Li, J.; Jaouen, F. Structure and activity of metal-centered coordination sites in pyrolyzed metal–nitrogen–carbon catalysts for the electrochemical reduction of O2. *Curr. Opin. Electrochem.* **2018**, *9*, 198-206. DOI: 10.1016/j.coelec.2018.03.039.

16. Kato, M.; Yagi, I. Electrocatalytic Oxygen Reduction at Multinuclear Metal Active Sites Inspired by Metalloenzymes. *e-J. Surf. Sci. Nanotechnol.* **2020**, *18*, 81-93. DOI: 10.1380/ejssnt.2020.81.
17. Banham, D.; Ye, S.; Pei, K.; Ozaki, J.-i.; Kishimoto, T.; Imashiro, Y. A review of the stability and durability of non-precious metal catalysts for the oxygen reduction reaction in proton exchange membrane fuel cells. *J. Power Sources* **2015**, *285*, 334-348. DOI: 10.1016/j.jpowsour.2015.03.047.
18. Sahraie, N. R.; Kramm, U. I.; Steinberg, J.; Zhang, Y.; Thomas, A.; Reier, T.; Paraknowitsch, J.-P.; Strasser, P. Quantifying the density and utilization of active sites in non-precious metal oxygen electroreduction catalysts. *Nature Commun.* **2015**, *6*, 8618. DOI: 10.1038/ncomms9618.
19. Zhang, D.; Chen, W.; Li, Z.; Chen, Y.; Zheng, L.; Gong, Y.; Li, Q.; Shen, R.; Han, Y.; Cheong, W.-C.; Gu, L.; Li, Y. Isolated Fe and Co dual active sites on nitrogen-doped carbon for a highly efficient oxygen reduction reaction. *Chem. Commun.* **2018**, *54*, 4274-4277. DOI: 10.1039/C8CC00988K.
20. Wang, J.; Liu, W.; Luo, G.; Li, Z.; Zhao, C.; Zhang, H.; Zhu, M.; Xu, Q.; Wang, X.; Zhao, C.; Qu, Y.; Yang, Z.; Yao, T.; Li, Y.; Lin, Y.; Wu, Y.; Li, Y. Synergistic effect of well-defined dual sites boosting the oxygen reduction reaction. *Energy Environ. Sci.* **2018**, *11*, 3375-3379. DOI: 10.1039/C8EE02656D.
21. Zhu, Z.; Yin, H.; Wang, Y.; Chuang, C.-H.; Xing, L.; Dong, M.; Lu, Y.-R.; Casillas-Garcia, G.; Zheng, Y.; Chen, S.; Dou, Y.; Liu, P.; Cheng, Q.; Zhao, H. Coexisting Single-Atomic Fe and Ni Sites on Hierarchically Ordered Porous Carbon as a Highly Efficient ORR Electrocatalyst. *Adv. Mater.* **2020**, *32*, 2004670. DOI: 10.1002/adma.202004670.
22. Kato, M.; Murotani, T.; Yagi, I. Bioinspired Iron- and Copper-incorporated Carbon Electrocatalysts for Oxygen Reduction Reaction. *Chem. Lett.* **2016**, *45*, 1213-1215. DOI: 10.1246/cl.160573.
23. He, Q.; Yang, X.; Ren, X.; Koel, B. E.; Ramaswamy, N.; Mukerjee, S.; Kostecki, R. A novel CuFe-based catalyst for the oxygen reduction reaction in alkaline media. *J. Power Sources* **2011**, *196*, 7404-7410. DOI: 10.1016/j.jpowsour.2011.04.016.
24. Kang, Y. S.; Heo, Y.; Jung, J. Y.; Sohn, Y.; Lee, S. H.; Jang, J. H.; Kim, P.; Yoo, S. J. Highly active bimetallic CuFe-N-C electrocatalysts for oxygen reduction reaction in alkaline media. *J. Ind. Eng. Chem.* **2019**, *71*, 234-241. DOI: 10.1016/j.jiec.2018.11.031.
25. Li, J.; Chen, J.; Wan, H.; Xiao, J.; Tang, Y.; Liu, M.; Wang, H. Boosting oxygen reduction activity of Fe-N-C by partial copper substitution to iron in Al-air batteries. *Appl. Catal. B-Environ.* **2019**, *242*, 209-217. DOI: 10.1016/j.apcatb.2018.09.044.
26. Onoda, A.; Tanaka, Y.; Matsumoto, K.; Ito, M.; Sakata, T.; Yasuda, H.; Hayashi, T. Bimetallic M/N/C catalysts prepared from π-expanded metal salen precursors toward an efficient oxygen reduction reaction. *RSC Adv.* **2018**, *8*, 2892-2899. DOI: 10.1039/C7RA12657C.
27. Qiao, Y.; Ni, Y. Y.; Kong, F. T.; Li, R. J.; Zhang, C. Q.; Kong, A. G.; Shan, Y. K. Pyrolytic Carbon-coated Cu-Fe Alloy Nanoparticles with High Catalytic Performance for Oxygen Electroreduction. *Chem. Asian J.* **2019**, *14*, 2676-2684. DOI: 10.1002/asia.201900524.
28. Serov, A.; Robson, M. H.; Smolnik, M.; Atanassov, P. Templated bi-metallic non-PGM catalysts for oxygen reduction. *Electrochim. Acta* **2012**, *80*, 213-218. DOI: 10.1016/j.electacta.2012.07.008.
29. He, Q. G.; Yang, X. F.; He, R. H.; Bueno-Lopez, A.; Miller, H.; Ren, X. M.; Yang, W. L.; Koel, B. E. Electrochemical and spectroscopic study of novel Cu and Fe-based catalysts for

oxygen reduction in alkaline media. *J. Power Sources* **2012**, *213*, 169-179. DOI: 10.1016/j.jpowsour.2012.04.029.
30. Ishii, T.; Maie, T.; Hamano, M.; Kishimoto, T.; Mizushiri, M.; Imashiro, Y.; Ozaki, J.-i. Synergistically enhanced oxygen reduction activity of iron-based nanoshell carbons by copper incorporation. *Carbon* **2017**, *116*, 591-598. DOI: 10.1016/j.carbon.2017.02.035.
31. Zhang, J.; Yang, H.; Liu, B. Coordination Engineering of Single-Atom Catalysts for the Oxygen Reduction Reaction: A Review. *Adv. Energy Mater. n/a*, 2002473. DOI: 10.1002/aenm.202002473.
32. Ying, Y.; Luo, X.; Qiao, J.; Huang, H. "More is Different:" Synergistic Effect and Structural Engineering in Double-Atom Catalysts. *Adv. Funct. Mater. n/a*, 2007423. DOI: 10.1002/adfm.202007423.
33. Wang, X.; Clément, R.; Roger, M.; Bauzan, M.; Mazurenko, I.; Poulpiquet, A. d.; Ilbert, M.; Lojou, E. Bacterial Respiratory Chain Diversity Reveals a Cytochrome c Oxidase Reducing O2 at Low Overpotentials. *J. Am. Chem. Soc.* **2019**, *141*, 11093-11102. DOI: 10.1021/jacs.9b03268.
34. Bhagi-Damodaran, A.; Michael, M. A.; Zhu, Q.; Reed, J.; Sandoval, B. A.; Mirts, E. N.; Chakraborty, S.; Moënne-Loccoz, P.; Zhang, Y.; Lu, Y. Why copper is preferred over iron for oxygen activation and reduction in haem-copper oxidases. *Nature Chem.* **2016**, *9*, 257-263. DOI: 10.1038/nchem.2643.
35. Collman, J. P.; Devaraj, N. K.; Decréau, R. A.; Yang, Y.; Yan, Y.-L.; Ebina, W.; Eberspacher, T. A.; Chidsey, C. E. D. A Cytochrome c Oxidase Model Catalyzes Oxygen to Water Reduction Under Rate-Limiting Electron Flux. *Science* **2007**, *315*, 1565-1568. DOI: 10.1126/science.1135844.
36. Babcock, G. T.; Wikström, M. Oxygen activation and the conservation of energy in cell respiration. *Nature* **1992**, *356*, 301-309. DOI: 10.1038/356301a0.
37. Chatterjee, S.; Sengupta, K.; Hematian, S.; Karlin, K. D.; Dey, A. Electrocatalytic O2-Reduction by Synthetic Cytochrome c Oxidase Mimics: Identification of a "Bridging Peroxo" Intermediate Involved in Facile 4e–/4H+ O2-Reduction. *J. Am. Chem. Soc.* **2015**, *137*, 12897-12905. DOI: 10.1021/jacs.5b06513.
38. Adam, S. M.; Garcia-Bosch, I.; Schaefer, A. W.; Sharma, S. K.; Siegler, M. A.; Solomon, E. I.; Karlin, K. D. Critical Aspects of Heme–Peroxo–Cu Complex Structure and Nature of Proton Source Dictate Metal–Operoxo Breakage versus Reductive O–O Cleavage Chemistry. *J. Am. Chem. Soc.* **2017**, *139*, 472-481. DOI: 10.1021/jacs.6b11322.
39. Kitagishi, H.; Shimoji, D.; Ohta, T.; Kamiya, R.; Kudo, Y.; Onoda, A.; Hayashi, T.; Weiss, J.; Wytko, J. A.; Kano, K. A water-soluble supramolecular complex that mimics the heme/copper hetero-binuclear site of cytochrome c oxidase. *Chem. Sci.* **2018**, *9*, 1989-1995. DOI: 10.1039/C7SC04732K.
40. Adam, S. M.; Wijeratne, G. B.; Rogler, P. J.; Diaz, D. E.; Quist, D. A.; Liu, J. J.; Karlin, K. D. Synthetic Fe/Cu Complexes: Toward Understanding Heme-Copper Oxidase Structure and Function. *Chem. Rev.* **2018**, *118*, 10840-11022. DOI: 10.1021/acs.chemrev.8b00074.
41. Muthukrishnan, A.; Nabae, Y. Estimation of the Inherent Kinetic Parameters for Oxygen Reduction over a Pt-Free Cathode Catalyst by Resolving the Quasi-Four-Electron Reduction. *J. Phys. Chem. C* **2016**, *120*, 22515-22525. DOI: 10.1021/acs.jpcc.6b07905.
42. Wu, Y.; Nagata, S.; Nabae, Y. Genuine four-electron oxygen reduction over precious-metal-free catalyst in alkaline media. *Electrochim. Acta* **2019**, *319*, 382-389. DOI: 10.1016/j.electacta.2019.06.174.

43. Tse, E. C. M.; Varnell, J. A.; Hoang, T. T. H.; Gewirth, A. A. Elucidating Proton Involvement in the Rate-Determining Step for Pt/Pd-Based and Non-Precious-Metal Oxygen Reduction Reaction Catalysts Using the Kinetic Isotope Effect. *J. Phys. Chem. Lett.* **2016**, *7*, 3542-3547. DOI: 10.1021/acs.jpclett.6b01235.
44. Liang, Z.-X.; Song, H.-Y.; Liao, S.-J. Hemin: A Highly Effective Electrocatalyst Mediating the Oxygen Reduction Reaction. *J. Phys. Chem. C* **2011**, *115*, 2604-2610. DOI: 10.1021/jp1112334.
45. Yamada, T.; Maruta, G.; Takeda, S. Reversible solid-state structural conversion between a three-dimensional network and a one-dimensional chain of Cu(II) triazole coordination polymers in acidic/basic-suspensions or vapors. *Chem. Commun.* **2011**, *47*, 653-655. DOI: 10.1039/C0CC04293E.
46. Kato, M.; Muto, M.; Matsubara, N.; Uemura, Y.; Wakisaka, Y.; Yoneuchi, T.; Matsumura, D.; Ishihara, T.; Tokushima, T.; Noro, S.-i.; Takakusagi, S.; Asakura, K.; Yagi, I. Incorporation of Multinuclear Copper Active Sites into Nitrogen-Doped Graphene for Electrochemical Oxygen Reduction. *ACS Appl. Energy Mater.* **2018**, *1*, 2358-2364. DOI: 10.1021/acsaem.8b00491.
47. Sa, Y. J.; Seo, D.-J.; Woo, J.; Lim, J. T.; Cheon, J. Y.; Yang, S. Y.; Lee, J. M.; Kang, D.; Shin, T. J.; Shin, H. S.; Jeong, H. Y.; Kim, C. S.; Kim, M. G.; Kim, T.-Y.; Joo, S. H. A General Approach to Preferential Formation of Active Fe–Nx Sites in Fe–N/C Electrocatalysts for Efficient Oxygen Reduction Reaction. *J. Am. Chem. Soc.* **2016**, *138*, 15046-15056. DOI: 10.1021/jacs.6b09470.
48. Kato, M.; Oyaizu, N.; Shimazu, K.; Yagi, I. Oxygen Reduction Reaction Catalyzed by Self-Assembled Monolayers of Copper-Based Electrocatalysts on a Polycrystalline Gold Surface. *J. Phys. Chem. C* **2016**, *120*, 15814-15822. DOI: 10.1021/acs.jpcc.5b11663.
49. Wu, Y.; Nabae, Y. Rotating ring-disk electrode theory and method to correct quasi-four-electron oxygen reduction over Fe/N/C and N/C cathode catalysts. *Curr. Opin. Electrochem.* **2021**, *25*, 100633. DOI: 10.1016/j.coelec.2020.08.015.
50. Zhang, H.; Chung, H. T.; Cullen, D. A.; Wagner, S.; Kramm, U. I.; More, K. L.; Zelenay, P.; Wu, G. High-performance fuel cell cathodes exclusively containing atomically dispersed iron active sites. *Energy Environ. Sci.* **2019**, *12*, 2548-2558. DOI: 10.1039/C9EE00877B.
51. Stamenkovic, V. R.; Strmcnik, D.; Lopes, P. P.; Markovic, N. M. Energy and fuels from electrochemical interfaces. *Nature Mater.* **2017**, *16*, 57-69. DOI: 10.1038/nmat4738.
52. Kato, M.; Nakahoshiba, R.; Ogura, K.; Tokuda, S.; Yasuda, S.; Higashi, K.; Uruga, T.; Uemura, Y.; Yagi, I. Electronic Effects of Nitrogen Atoms of Supports on Pt–Ni Rhombic Dodecahedral Nanoframes for Oxygen Reduction. *ACS Appl. Energy Mater.* **2020**, *3*, 6768-6774. DOI: 10.1021/acsaem.0c00903.
53. Clavilier, J. The role of anion on the electrochemical behaviour of a {111} platinum surface; an unusual splitting of the voltammogram in the hydrogen region. *J. Electroanal. Chem. Interf. Electrochem.* **1980**, *107*, 211-216. DOI: 10.1016/S0022-0728(79)80023-6.
54. Markovic, N. M.; Gasteiger, H. A.; Ross, P. N. Oxygen Reduction on Platinum Low-Index Single-Crystal Surfaces in Sulfuric Acid Solution: Rotating Ring-Pt(hkl) Disk Studies. *J. Phys. Chem.* **1995**, *99*, 3411-3415. DOI: 10.1021/j100011a001.
55. Gamboa-Aldeco, M. E.; Herrero, E.; Zelenay, P. S.; Wieckowski, A. Adsorption of bisulfate anion on a Pt(100) electrode: A comparison with Pt(111) and Pt(poly). *J. Electroanal. Chem.* **1993**, *348*, 451-457. DOI: 10.1016/0022-0728(93)80151-7.
56. Yano, H.; Uematsu, T.; Omura, J.; Watanabe, M.; Uchida, H. Effect of adsorption of sulfate anions on the activities for oxygen reduction reaction on Nafion (R)-coated Pt/carbon black

catalysts at practical temperatures. *J. Electroanal. Chem.* **2015**, *747*, 91-96. DOI: 10.1016/j.jelechem.2015.04.007.
57. Kinumoto, T.; Inaba, M.; Nakayama, Y.; Ogata, K.; Umebayashi, R.; Tasaka, A.; Iriyama, Y.; Abe, T.; Ogumi, Z. Durability of perfluorinated ionomer membrane against hydrogen peroxide. *J. Power Sources* **2006**, *158*, 1222-1228. DOI: 10.1016/j.jpowsour.2005.10.043.
58. Liang, Z.; Luo, M.; Chen, M.; Liu, C.; Peera, S. G.; Qi, X.; Liu, J.; Kumar, U. P.; Liang, T. L. T. Evaluating the catalytic activity of transition metal dimers for the oxygen reduction reaction. *J. Colloid Interf. Sci.* **2020**, *568*, 54-62. DOI: 10.1016/j.jcis.2020.02.034.
59. Deng, C.; Su, Y.; Li, F.; Shen, W.; Chen, Z.; Tang, Q. Understanding activity origin for the oxygen reduction reaction on bi-atom catalysts by DFT studies and machine-learning. *J. Mater. Chem. A* **2020**, *8*, 24563-24571. DOI: 10.1039/D0TA08004G.
60. Nicolay, A.; Tilley, T. D. Selective Synthesis of a Series of Isostructural $M^{II}Cu^{I}$ Heterobimetallic Complexes Spontaneously Assembled by an Unsymmetrical Naphthyridine-Based Ligand. *Chem. Eur. J.* **2018**, *24*, 10329-10333. DOI: 10.1002/chem.201802623.
61. Primbs, M.; Sun, Y.; Roy, A.; Malko, D.; Mehmood, A.; Sougrati, M.-T.; Blanchard, P.-Y.; Granozzi, G.; Kosmala, T.; Daniel, G.; Atanassov, P.; Sharman, J.; Durante, C.; Kucernak, A.; Jones, D.; Jaouen, F.; Strasser, P. Establishing reactivity descriptors for platinum group metal (PGM)-free Fe–N‑C catalysts for PEM fuel cells. *Energy Environ. Sci.* **2020**, *13*, 2480-2500. DOI: 10.1039/D0EE01013H.
62. Ramaswamy, N.; Tylus, U.; Jia, Q.; Mukerjee, S. Activity Descriptor Identification for Oxygen Reduction on Nonprecious Electrocatalysts: Linking Surface Science to Coordination Chemistry. *J. Am. Chem. Soc.* **2013**, *135*, 15443-15449. DOI: 10.1021/ja405149m.
63. Kramm, U. I.; Herranz, J.; Larouche, N.; Arruda, T. M.; Lefèvre, M.; Jaouen, F.; Bogdanoff, P.; Fiechter, S.; Abs-Wurmbach, I.; Mukerjee, S.; Dodelet, J.-P. Structure of the catalytic sites in Fe/N/C-catalysts for O2-reduction in PEM fuel cells. *Phys. Chem. Chem. Phys.* **2012**, *14*, 11673-11688. DOI: 10.1039/C2CP41957B.
64. Gasteiger, H. A.; Kocha, S. S.; Sompalli, B.; Wagner, F. T. Activity benchmarks and requirements for Pt, Pt-alloy, and non-Pt oxygen reduction catalysts for PEMFCs. *Appl. Catal. B* **2005**, *56*, 9-35. DOI: 10.1016/j.apcatb.2004.06.021.
65. Zitolo, A.; Goellner, V.; Armel, V.; Sougrati, M.-T.; Mineva, T.; Stievano, L.; Fonda, E.; Jaouen, F. Identification of catalytic sites for oxygen reduction in iron- and nitrogen-doped graphene materials. *Nature Mater.* **2015**, *14*, 937. DOI: 10.1038/nmat4367.

SYNOPSIS.